

Phonon and defect mediated quantum anomalous Hall insulator to metal transition in magnetically doped topological insulators

Akiyoshi Park ^{1,2}, Adrian Llanos,² Chun-I Lu ¹, Yinan Chen ^{1,2}, Sebastien N. Abadi ¹, Chien-Chang Chen,^{1,2} Marcus L. Teague,^{1,2} Lixuan Tai ³, Peng Zhang ³, Kang L. Wang,³ and Nai-Chang Yeh ^{1,2,*}

¹*Department of Physics, California Institute of Technology, Pasadena, California 91125, USA*

²*Institute for Quantum Information and Matter, California Institute of Technology, Pasadena, California 91125, USA*

³*Department of Electrical Engineering, University of California, Los Angeles, California 90095, USA*



(Received 3 October 2023; accepted 19 January 2024; published 12 February 2024)

Quantum anomalous Hall (QAH) state in six quintuple layer $\text{Cr}_{0.1}(\text{Bi}_{0.2}\text{Sb}_{0.8})_{1.9}\text{Te}_3$ thin films were studied through scanning tunneling spectroscopy (STS) and electrical transport measurements. While the surface state is gapless above the Curie temperature ($T_C \approx 30$ K), scanning tunneling spectroscopy (STS) of the sample reveals a topologically nontrivial gap with an average value of ≈ 13.5 meV at 4.2 K below the ferromagnetic transition. Nonetheless, areal STS scans of the magnetic topological insulator exhibit energy modulations on the order of several meV's in the surface bands, which result in the valence band maximum in some regions becoming higher than the energy of the conduction band minimum of some other regions that are spatially separated by no more than 3 nm. First-principles calculations demonstrate that the origin of the observed inhomogeneous energy band alignment is an outcome of many-body interactions, namely electron-defect interactions and electron-phonon interactions. Defects play the role of locally modifying the energy landscape of surface bands while electron-phonon interactions renormalize the surface bands such that the surface gap becomes reduced by more than 1 meV as temperature is raised from 0 to 4.2 K. These many-body interactions at a finite temperature result in substantial increase of electron tunneling across the spatially separated conduction band pockets even for finite temperatures well below T_C , thus driving the magnetic topological insulator out of its QAH insulating phase into a metallic phase at a relatively low temperature.

DOI: [10.1103/PhysRevB.109.075125](https://doi.org/10.1103/PhysRevB.109.075125)

I. INTRODUCTION

Experimental observations of the quantum anomalous Hall effect (QAHE) among Cr-doped $(\text{Bi}, \text{Sb})_2\text{Te}_3$, a system of magnetic topological insulators (MTIs), have been bound to below sub-Kelvin temperatures [1–3]. Such constraint of the QAHE to low temperatures is unexpected given that these MTIs exhibit long-range ferromagnetic ordering at much higher temperatures [4]. Specifically, transport measurements of Cr-doped $(\text{Bi}, \text{Sb})_2\text{Te}_3$ have shown bulk Curie temperatures (T_C) ranging from 20–30 K, whereas the appearance of QAHE has been limited to temperatures below 0.1 K [4].

It has been proclaimed that the bottleneck in the temperature range of the QAHE is the lack of spatially homogeneous ferromagnetic ordering such that the region with gapped topological surface states is beneath the percolation threshold at higher temperatures [5–8]. Nonetheless, significantly improved magnetic homogeneity using either magnetic modulation doping in heterostructures [9] or codoping Cr with V atoms [10] could only raise the threshold temperature for QAHE to approximately 2 K.

Fundamentally for QAHE to ensue, the effective Zeeman field emanating from ferromagnetic ordering closes the topologically trivial hybridization gap through band inversion and opens up a nontrivial magnetic gap, thus creating a Chern

insulator phase characterized by the topological invariant, $C = \pm 1$, referred to as the Chern number. Although some experiments have reported the presence of the magnetic gap opening in the surface states of MTIs [7,11–14], there are contradictory results that indicate otherwise [15,16]. There are also reports of opening of a topological nontrivial gap being masked by midgapped impurity states [17,18] or bulk states [19]. In addition, it has been argued that the Dirac point in MTIs is degenerate with the bulk valence band, thereby compromising the conductivity [20,21]. Hence, the issue regarding whether magnetic doped $(\text{Bi}, \text{Sb})_2\text{Te}_3$ are true topological insulators has not been settled.

In particular, the lack of general agreement among reports concerning the electronic structure of these materials is attributed to inadequate distinctions between MTI samples in the bulk and the two-dimensional (2D) limit. The two are fundamentally different, given that the QAHE has only been observed in epitaxial films [6,21,22]. The absence of quantized transport in bulk single crystal is attributed to higher defect concentration such that the chemical potential falls outside the surface gap [7,23], and a larger structural inversion asymmetry that appears to be an obstacle for a topological phase transition to the Chern insulator state [24]. The lack of a consensus thus calls for a more thorough investigation to map out the energies of the surface and bulk electronic states above and below the topological phase transition temperature in 2D MTI-epitaxial films, which duly exhibit a QAH phase.

*Corresponding author: ncyeh@caltech.edu

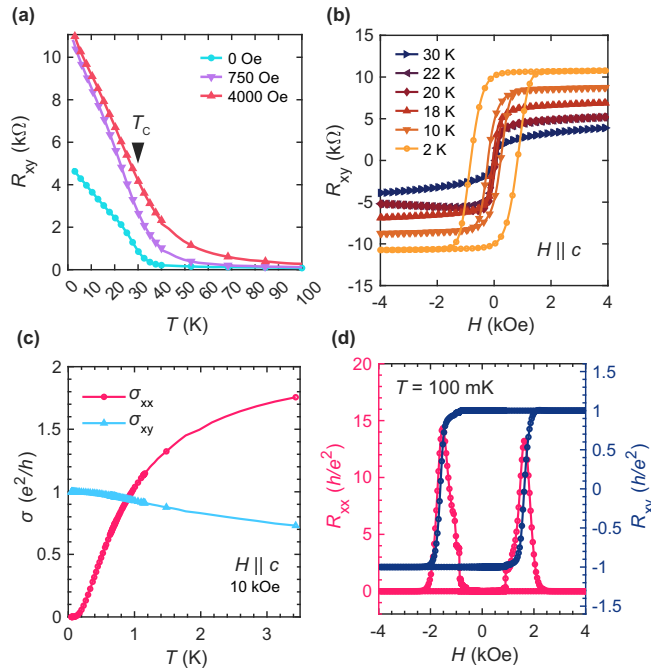


FIG. 1. Temperature and magnetic field dependence of longitudinal and Hall resistance in $\text{Cr}_{0.1}(\text{Bi}_{0.2}\text{Sb}_{0.8})_{1.9}\text{Te}_3$ (a) The temperature dependence of R_{xy} measured at various magnetic fields. A rapid increase in zero-field R_{xy} appears around $T = 30$ K, suggesting the onset of ferromagnetism. (b) Hysteric behavior in R_{xy} dependence of magnetic field (H) at different temperatures between 30 K and 2 K. (c) σ_{xy} and σ_{xx} upon field cooling with $H = 10$ kOe exhibiting QAHE at $T = 100$ mK. (d) Magnetic field sweep of R_{xy} and R_{xx} at $T = 100$ mK.

II. EXPERIMENTAL AND COMPUTATIONAL METHODS

A. Sample growth

$\text{Cr}_y(\text{Bi}_{1-x}\text{Sb}_x)_{2-y}\text{Te}_3$ thin films with an average thickness of six quintuple layers (QLs) were grown by molecular beam epitaxy (MBE) on (111) GaAs substrates in an ultrahigh vacuum Perkin-Elmer instrument. The details of the method have been outlined in Ref. [21]. The thickness of the sample is determined through the oscillation of reflection high-energy electron diffraction (RHEED) patterns over the growth process.

Although there are terracelike structures and thickness variation over different regions of on the thin film [Fig. 2(a)], the average thickness is determined to be six QLs, which is sufficiently thick to suppress the hybridization gap between the bottom and top surface states to ≈ 5 meV, but still thin enough to reduce the effect of structural inversion asymmetry that prevents band inversion to a topological nontrivial phase [25,26].

B. Scanning tunneling microscopy/spectroscopy

Scanning tunneling microscopy/spectroscopy (STM/STS) measurements were performed in a homemade microscope connected to a RHK R9 controller. To achieve liquid helium temperatures, small traces of ultrahigh purity He (99.999%) exchange gas were added to the vacuum chamber. Tunneling

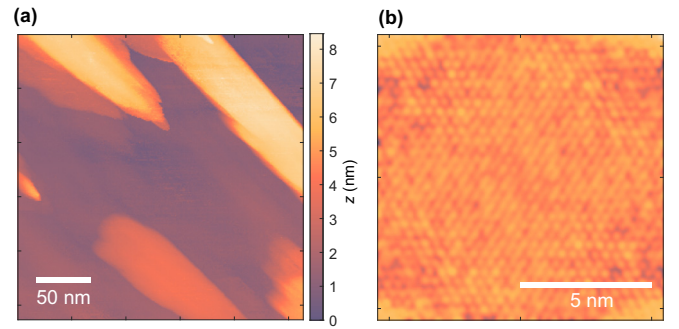


FIG. 2. STM Topographic images at $T = 4.2$ K. (a) Images of terracelike structures were observed over a larger area of ($300 \text{ nm} \times 300 \text{ nm}$) due to the layered nature of $\text{Cr}_{0.1}(\text{Bi}_{0.2}\text{Sb}_{0.8})_{1.9}\text{Te}_3$, obtained with scanning parameters of $I_t = 100$ pA and $V_b = 1$ V. (b) A smaller area of ($11 \text{ nm} \times 11 \text{ nm}$), where individual atoms were resolved with scanning parameter of $I_t = 1$ nA and $V_b = 100$ mV. The atomic scale image is processed through Fourier filtering to improve the signal-to-noise ratio of the image.

spectroscopy was measured through an ac lock-in amplifier with a bias modulation of 10 mV amplitude. Mechanically cleaved Pt-Ir alloy wires were used as the STM tips.

C. Transport measurements

Thin film samples for transport measurements were first patterned into a Hall bar geometry. Temperature and magnetic field dependence of longitudinal and Hall resistance was measured by using a Physical Property Measurement System (PPMS) by Quantum Design. Three SRS SR830 Lock-in Amplifiers were employed: two were used to monitor the Hall voltage and the longitudinal voltage, and one was used to supply a current by applying an ac voltage of $V_{\text{rms}} = 10$ mV and frequency between $f = 5\text{--}15$ Hz across a $1 \text{ M}\Omega$ reference resistor.

D. First-principles calculations

Density functional theory (DFT) calculations were performed by QUANTUM ESPRESSO (QE) using a fully relativistic pseudopotential and setting up noncollinear calculations to incorporate the effects of spin-orbit coupling [27,28]. For calculating the electronic structure of the parent compound Sb_2Te_3 , initially a $(4 \times 4 \times 1)$ k -point mesh was constructed to obtain self-consistent electron densities through self-consistent field (SCF) calculations followed by non-self-consistent field (NCF) calculations to obtain eigenvalues of a finer $(40 \times 40 \times 1)$ k -point mesh.

Furthermore, to implement and investigate various perturbative disorder to topological insulators such as defects, magnetic dopants, and electron-phonon coupling, which break translational lattice symmetry, a change from reciprocal-space to real-space basis is required. This was performed through using Bloch states obtained from QE to construct a real-space lattice Hamiltonian by computing maximally localized Wannier functions (MLWFs) via the WANNIER90 package [29]. For each atom in the unit cell, initial projections were represented as p_x , p_y , and p_z orbitals with spin up and down, given that the p orbitals of (Bi,Sb) and Te are the most relevant bands lying

close to the Fermi level (E_F) [30]. Hence, a three-QL unit cell consisting of 30 atoms would yield a (90×90) -matrix Hamiltonian, and a (180×180) -matrix Hamiltonian for a six-QL unit cell.

The electronic structures of the doped system were calculated through construction of supercells with various doping configurations. The supercell band structures were determined through SCF and NCF calculations using QE followed by Wannierization, as with the case for the unit cell calculations. Since the Brillouin zone (BZ) of the supercell is smaller than the BZ of the unit cell, an extra step of band unfolding was necessitated, which was done through the WANNIERTOOLS postprocessing software [31].

To realize the effects of finite temperatures, electron-phonon coupling calculations were performed through a density functional perturbation theory (DFPT) approach. Dynamical matrices were computed using the phonon module in QE for a $(3 \times 3 \times 1)$ q -point mesh. The electron-phonon coupling parameters were then calculated up to the linear response regime through the electron-phonon Wannier (EPW) code using the dynamical matrices computed from QE [32].

III. RESULTS

A. Sample characterization

Six-QL $\text{Cr}_y(\text{Bi}_{1-x}\text{Sb}_x)_{2-y}\text{Te}_3$ thin films investigated in this work consist of a Cr-doping level of $y = 0.10$, which is the optimal doping for ferromagnetic order [21], and a Sb-doping level of $x = 0.80$ to tune the Fermi energy (E_F) right at the Dirac point (E_D) [1,33]. The presence of bulk ferromagnetic order due to Cr doping is manifested by the emergence of a finite Hall resistance (R_{xy}) across the sample upon zero-field cooling below T_C at approximately 30 K [Fig. 1(a)], indicative of time-reversal symmetry breaking. The bulk ferromagnetism below T_C is further verified by the opening of a hysteresis loop in the field-dependent Hall resistance data [Fig. 1(b)], which reveals a finite coercive field (H_C) that decreases with increasing temperature and diminishes to zero at approximately 30 K. At an even lower temperature of $T = 100$ mK, σ_{xy} reaches a quantized value of e^2/h , while the longitudinal resistivity (σ_{xx}) is suppressed to zero [Figs. 1(c) and 1(d)], verifying that the sample is indeed a QAH insulator.

Large area STM topographic images indicate that the sample surface is atomically flat, exhibiting islands with terracelike features [Fig. 2(a)], whereas atomically resolved images in smaller areas reveal a triangular lattice pattern, representative of the crystalline structure of $(\text{Bi}, \text{Sb})_2\text{Te}_3$ in the ab plane. Noticeably, the unevenness in the topography over a nm scale represented by the darker color patches in Fig. 2(b) may be attributed to collective contributions from Bi/Sb alloying [34], Cr dopants (with an atomic radius much smaller than those of Bi and Sb atoms), or dilute crystalline defects, including interstitial and vacancies.

To understand the change in the properties of the samples across the ferromagnetic transition, where time-reversal symmetry is broken, scanning tunneling spectroscopy (STS) was performed both above T_C at liquid nitrogen temperature (77 K) and below T_C at liquid helium temperature (4.2 K).

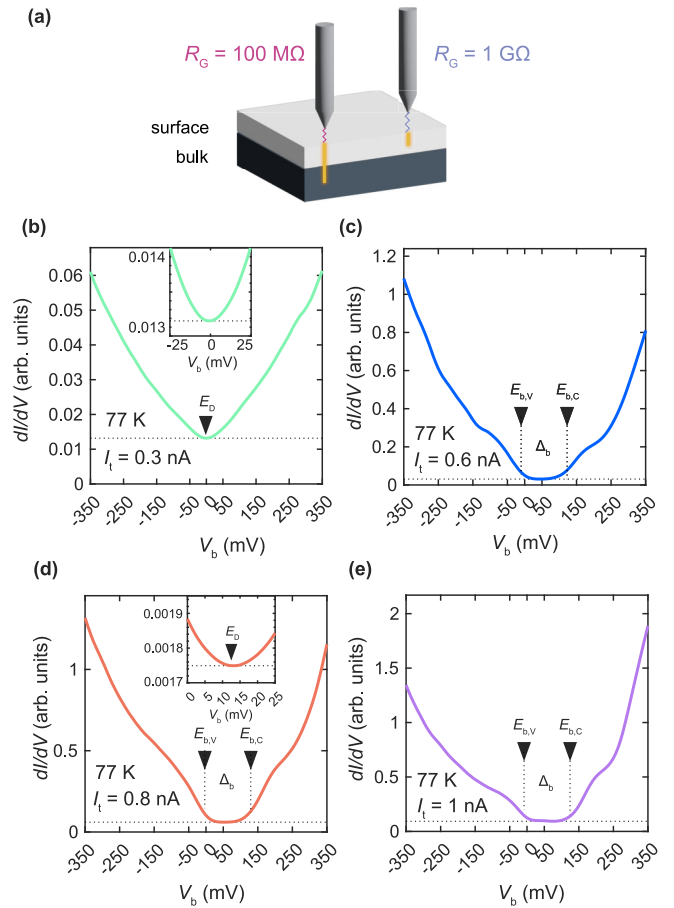


FIG. 3. Scanning tunneling spectra taken with different tunneling resistance at $T = 77$ K. (a) Schematic representation of tip-sample distance changing as a consequence of changing the tunneling resistance from $100 \text{ M}\Omega$ to $1 \text{ G}\Omega$. The higher the tunneling current, the closer the tip-sample distance in which the point spectra were measured. (b)–(e) Tunneling resistance-dependent point spectra were obtained with a fixed bias of $V_b = 100$ mV and variable tunneling currents of $I_t = 300$ pA, $I_t = 600$ pA, $I_t = 800$ pA, $I_t = 1000$ pA. The horizontal dotted lines are the baselines, which indicate the minima of each spectrum. The insets exhibit the low-energy region of the spectra with the corresponding Dirac point.

B. STM investigation above the Curie temperature

Information associated with the local density of states (LDOS) is acquired by conducting differential conductance (dI/dV) spectroscopy, in which the height of the STM tip relative to the sample surface is kept constant while measuring the tunneling current (I_t) as a function of the bias voltage (V_b) between the sample and the tip with a lock-in amplifier. The spatial separation between the tip and the sample is determined by the tunneling resistance ($R_G = V_b/I_t$), where a higher R_G corresponds to a larger tip-sample separation [Fig. 3(a)]. Figures 3(b)–3(e) exhibit the tunneling spectra obtained from an atomically flat surface area at 77 K with varying R_G . With $R_G = 333 \text{ M}\Omega$ ($I_t = 300$ pA, $V_b = 100$ mV), a V-shaped energy dependence was evident from the dI/dV spectrum, which was representative of the Dirac surface states with the minimum dI/dV appearing at the E_D [Fig. 3(b)], and the finite LDOS at and around E_D indicates a

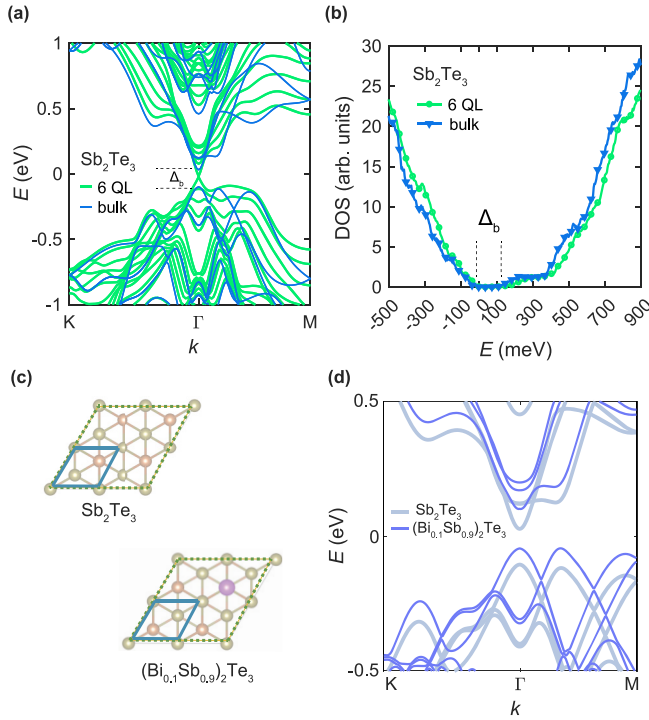


FIG. 4. Calculated electronic structure of $(\text{Bi,Sb})_2\text{Te}_3$ from DFT. (a) The band structure and (b) the DOS of Sb_2Te_3 with a bulk configuration and a six QL slab configuration. (c) Crystalline ab plane of a $2 \times 2 \times 1$ supercell for the parent compound, Sb_2Te_3 , and the doped compound, $(\text{Bi}_{0.1}\text{Sb}_{0.9})_2\text{Te}_3$. The dashed lines represent the supercell and the solid lines represent the unit cell. (d) The unfolded band structure of both Bi-doped and parent bulk supercell structure.

virtually gapless surface state as expected above T_C . Remarkably, E_D nearly coincides with the Fermi level (corresponding to $E = 0$ in the tunneling spectrum) [33], which is in stark contrast to most single-crystal samples with E_D more than 100 meV above E_F [7,23,35].

As R_G is reduced such that the STM tip is brought closer to the sample surface, the dI/dV curve loses its V-shaped spectrum and exhibits kinklike features [Figs. 3(c)–3(e)]. Particularly, at low energies near E_F , an energy region of vanishing LDOS is recognizable. This energy region of vanishing LDOS corresponds to the bulk band gap (Δ_b) [30], as suggested by band structure obtained by first-principles calculations (Fig. 4). When reducing the tunneling resistance, the STM tip is sufficiently close to the sample surface, such that electron tunneling is no longer restricted exclusively between the tip and the surface states, but also between the tip and the bulk states that are only a few atomic layers below the surface. Tuning R_G , accordingly, allows selectively probing either (both) the surface or (and) bulk states in the $\text{Cr}_{0.1}(\text{Bi}_{0.2}\text{Sb}_{0.8})_{1.9}\text{Te}_3$ thin films of our investigation [36].

Notably, the Dirac point is located within Δ_b [Fig. 3(d)], and the value of Δ_b quantified through STS is on the same energy scale as that calculated from first principles for the parent compound, Sb_2Te_3 as well as that of the doped $(\text{Bi}_{0.1}\text{Sb}_{0.9})_2\text{Te}_3$ compound [Fig. 4(d)]. Comparing the bulk band structure of Sb_2Te_3 and $(\text{Bi}_{0.1}\text{Sb}_{0.9})_2\text{Te}_3$, we note that the E_F value of the Bi-doped bulk band structure is 70 meV

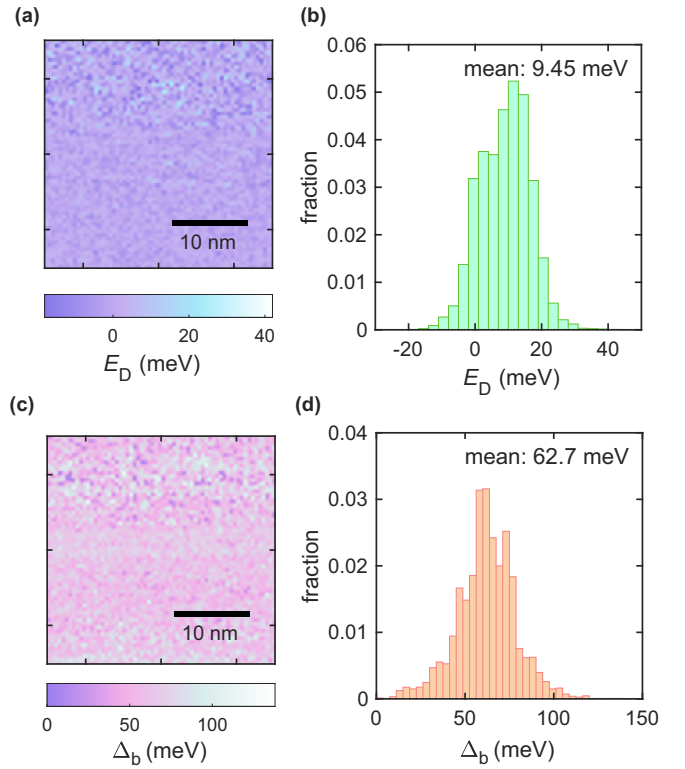


FIG. 5. Spatial distribution of $E_D(\vec{r})$ and $\Delta_b(\vec{r})$ at 77 K. (a) The spatial map of $E_D(\vec{r})$ measured at 77 K, (b) with the corresponding histogram. (c) The spatial map of $\Delta_b(\vec{r})$ measured at 77 K, (d) with the corresponding histogram.

higher than the E_F of the bulk band structure of the parent compound, owing to electron donation from the Bi atoms. Otherwise, the bulk band structures of the two compounds are nearly identical, with a consistent Δ_b .

Moreover, we address the issue of the absence of spectral evidence for the edge states near the step edges shown in Fig. 2(a). We attribute the lack of spectral characteristics of the edge state to local wave-function hybridization between the surface states above and below the step edge, similar to the finite-size effect encountered in the ultrathin film (< 6 QL) limit, which hinders the manifestation of spectral characteristics of the edge states at a step edge.

To evaluate the spatial distribution of $E_D(\vec{r})$ and $\Delta_b(\vec{r})$, the tunneling resistance was tuned to 167 M Ω ($I_t = 600$ pA, $V_b = 100$ mV), such that information from both the surface and the bulk are probed. With this fixed resistance, the dI/dV spectra were taken over a (30 nm \times 30 nm) area. The resulting distributions are depicted in Fig. 5. The average Dirac point lies at $\langle E_D(\vec{r}) \rangle = (9.45 \pm 7.52)$ meV, where the uncertainty here and henceforth represents the first standard deviation of the spatial variation. In this nm-scale scanned area, $E_D(\vec{r})$ has a narrow distribution, tightly bound to around E_F [Figs. 5(a) and 5(b)], further signifying how well the Bi/Sb doping was tuned in our samples to its ideal energy location to optimize the QAHE. In addition, the magnitude of the mean bulk band gap was at $\langle \Delta_b(\vec{r}) \rangle = (62.7 \pm 16.5)$ meV [Figs. 5(c) and 5(d)], with the mean energies of the bulk valence band maxima and the bulk conduction band minima being $\langle E_{b,v}(\vec{r}) \rangle =$

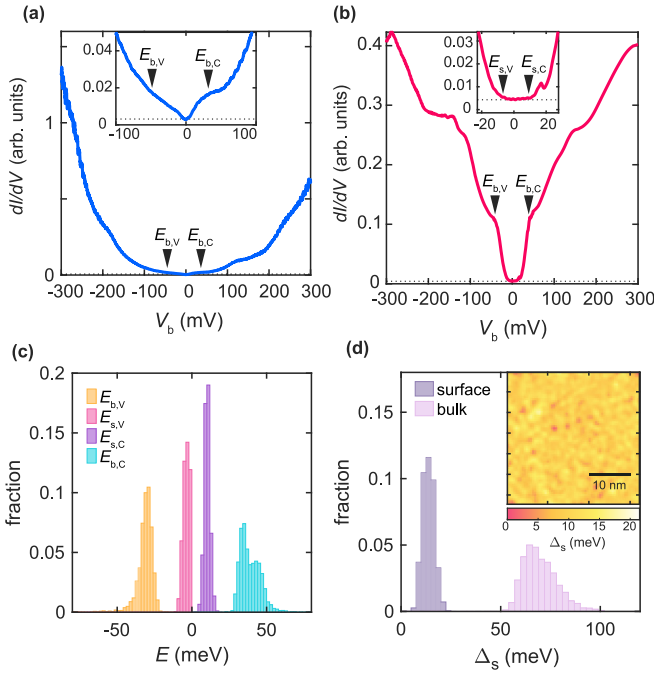


FIG. 6. Spatial distribution of $\Delta_s(\vec{r})$ at 4.2 K. (a) Representative STS measured at 4.2 K in which the tip's position was fixed with the bias voltage set at $V_b = 100$ mV and tunneling current set to (a) $I_t = 1000$ pA, and (b) $I_t = 200$ pA. The inset reveals a zoomed in spectra of the low-energy region. The horizontal dotted line is the baseline which indicates the minima of the spectra. (c) A histogram depicting the distribution of valence band maximum and conduction band minimum of the surface and bulk bands. (d) A histogram representing the distribution of $\Delta_s(\vec{r})$ and $\Delta_b(\vec{r})$. The inset exhibits the spatial map of $\Delta_s(\vec{r})$.

(-13.6 ± 16.5) meV and $\langle E_{b,C}(\vec{r}) \rangle = (48.8 \pm 12.9)$ meV, respectively. The spatial distribution maps of Figs. 5(a) and 5(c) reaffirm the statistical homogeneity on the nanometer scale.

C. STM investigation below the Curie temperature

Figures 6(a) and 6(b) exhibit representative dI/dV spectra within experimental resolution taken at a single point on an atomically flat surface at 4.2 K with two different tunneling resistances. As R_t is ramped from 100 M Ω [Fig. 6(a)] to 500 M Ω [Fig. 6(b)], the dI/dV spectrum evolves from displaying dominantly bulk states, to mainly the surface states, with traces of bulk-derived features at higher energies. In contrast to a linear dependence of the LDOS as seen in the spectrum taken at 77 K [Fig. 3(a)], the low-energy region of the spectrum in Fig. 6(b) (inset) reveals a small energy range with zero LDOS. Such a zero-conductance energy region in the surface bands is a characteristic of a gap formation. The appearance of the gap at 4.2 K, which was absent above T_C , advocates that the gap formation associated with the topologically nontrivial surface states is a consequence of global ferromagnetic order perpendicular to the ab plane [24].

To assess the spatial variations of the topological surface gap, a dI/dV scan over a (30 nm \times 30 nm) area was measured with tunneling parameters, $I_t = 200$ pA and

$V_b = 100$ mV. All dI/dV spectra at this tunneling resistance revealed features from both the bulk and surface states consistently throughout the area as represented in Fig. 6(b). The average bulk band gap measured in this area is $\langle \Delta_b \rangle(\vec{r}) = (75.2 \pm 8.94)$ meV, with $\langle E_{b,V}(\vec{r}) \rangle = (-39.3 \pm 28.6)$ meV and $\langle E_{b,C}(\vec{r}) \rangle = (45.8 \pm 31.7)$ meV [Figs. 6(c) and 6(d)]. The results obtained in this area at 4.2 K are consistent with those obtained in a different area at 77 K, except that the magnitude of the bulk gap at 4.2 K are marginally greater than that at 77 K, which is to be expected, due to reduced thermal smearing at lower temperatures.

The surface gap is quantified through placing a baseline at each spectrum. The two energies at which the lock-in amplifier current begins to rise above the background dark current of the STM ($I_{\text{dark}} = 1$ pA) from the baseline establish the upper and lower bounds of the surface gap. Such careful analysis reveals that the average surface band gap on this area is $\Delta_s(\vec{r}) = 13.5$ meV and the region is gapped throughout the area with no gapless sections [Figs. 6(c) and 6(d)]. The highly homogeneous long-range ferromagnetic order in this scanned area of the MBE-grown MTI thin film investigated here is therefore in stark contrast to the findings reported in Ref. [8], where a weakly interacting superparamagnetic domain of nanometer scale was observed. The surface gap values derived in this work are consistent with those reported in Refs. [37,38].

To further support the distinction made between the surface and the bulk gaps, momentum-dependent information is extracted from the dI/dV spatial maps by taking the tunneling conductance at a constant bias voltage for each pixel and then mapping out the conductance over a two-dimensional (2D) area. The top panels of Fig. 7 exemplify a constant bias LDOS maps at selected energies of $E = -150$ meV, -100 meV, -50 meV, 0 meV, 50 meV, and 100 meV. Noting that the local fluctuations in the LDOS at a constant energy represented standing waves of quasiparticle interferences induced by impurity scatterings from dopants and defects, 2D Fourier transformation of the LDOS spatial maps at constant energies yielded information about the impurity scattering wave vectors of quasiparticle interference (QPI) images in momentum space. The QPI images associated with the constant energy LDOS maps are shown in the bottom panels of Fig. 7, each exhibiting a single bright spot in the Γ point and six spots around it in the M direction.

For a full understanding of the correspondence between the scattering wave vectors and the patterns the QPI images, all possible scattering vectors on the Fermi surface, not only the intraband surface state scattering wave vectors (\vec{q}) but also the interband scattering wave vectors (\vec{Q}) between the surface and the bulk states, must be considered, given that spectral features associated with both the bulk and surface states were present in the dI/dV spectra (Fig. 6). In general, the prominent scattering vectors observed in QPI images are those scattering between pairs of momentum regions on the Fermi surface with high LDOS [39–42].

Figures 8(a)–8(g) indicate the theoretical momentum (\vec{k})-dependent constant energy LDOS maps of six-QL Sb_2Te_3 , which is a good approximation to six-QL $(\text{Bi}_{0.2}\text{Sb}_{0.8})_2\text{Te}_3$, obtained through density functional theory (DFT) calculations. There are three possible intraband scattering wave

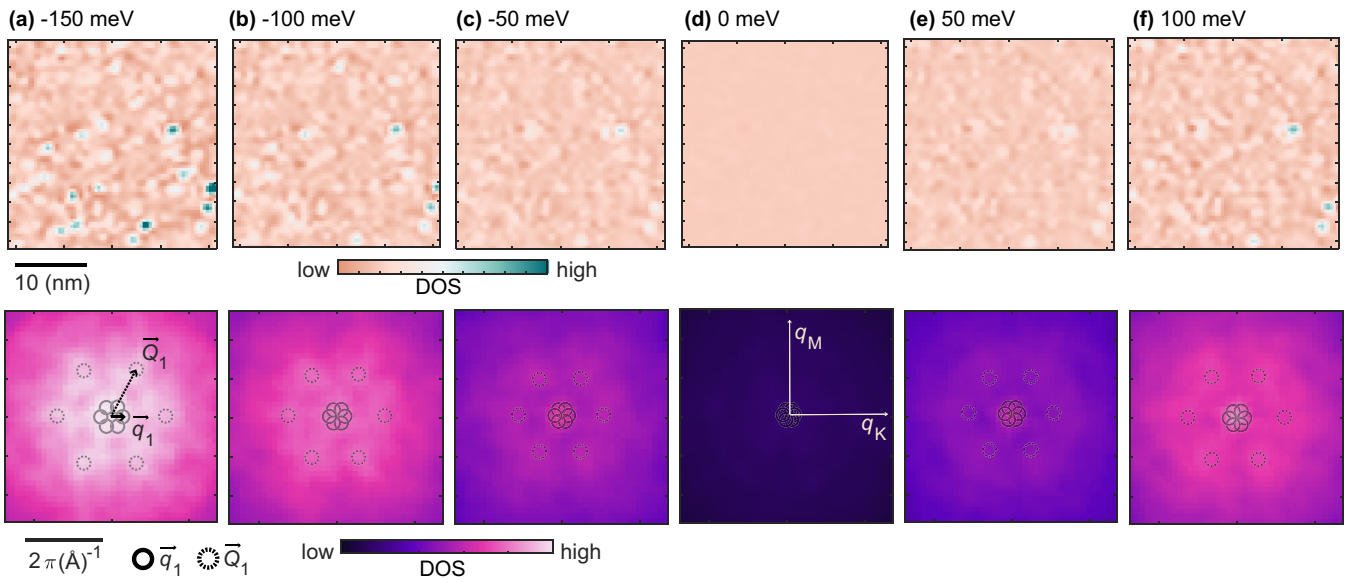


FIG. 7. dI/dV map at $T = 4.2$ K. The top row panels exhibit the constant bias conductance map and the bottom row indicate the Fourier transformed images (QPI maps) for (a) $E = -150$ meV, (b) $E = -100$ meV, (c) $E = -50$ meV, (d) $E = 0$ meV, (e) $E = 50$ meV, and (f) $E = 100$ meV. The color bars indicate the LDOS intensity.

vectors among the high LDOS regions on the surface band, which are denoted as \vec{q}_1 , \vec{q}_2 , and \vec{q}_3 , as shown in Figs. 8(c) and 8(f).

The scattering across the opposite nodes on the Dirac cone, \vec{q}_3 , is prohibited by Kramer's rule, and so can be excluded. Moreover, a previous STS study presented in Ref. [40] has indicated the absence of \vec{q}_2 and found \vec{q}_1 to be the prominent dominant intraband scattering in the surface bands. The diameter of the Dirac cone at 100 meV below E_D is approximately

0.05\AA^{-1} for Sb_2Te_3 as indicated by the DFT calculations [Fig. 8(c)] as well as the angle resolved photoemission spectrum (ARPES) measurements [43,44]. The scattering wave vector from the adjacent nodes of the hexagonal Dirac cone of the surface state at $E = -100$ meV is therefore approximately $\vec{q}_1 = 0.03 \text{\AA}^{-1}$ from Fig. 8(c). Hence, considering the scale of the scattering wave vectors, we associate the spots clustered around the Γ point along the Γ -M direction in the QPI image with the \vec{q}_1 scattering wave vectors [Fig. 7(c)].

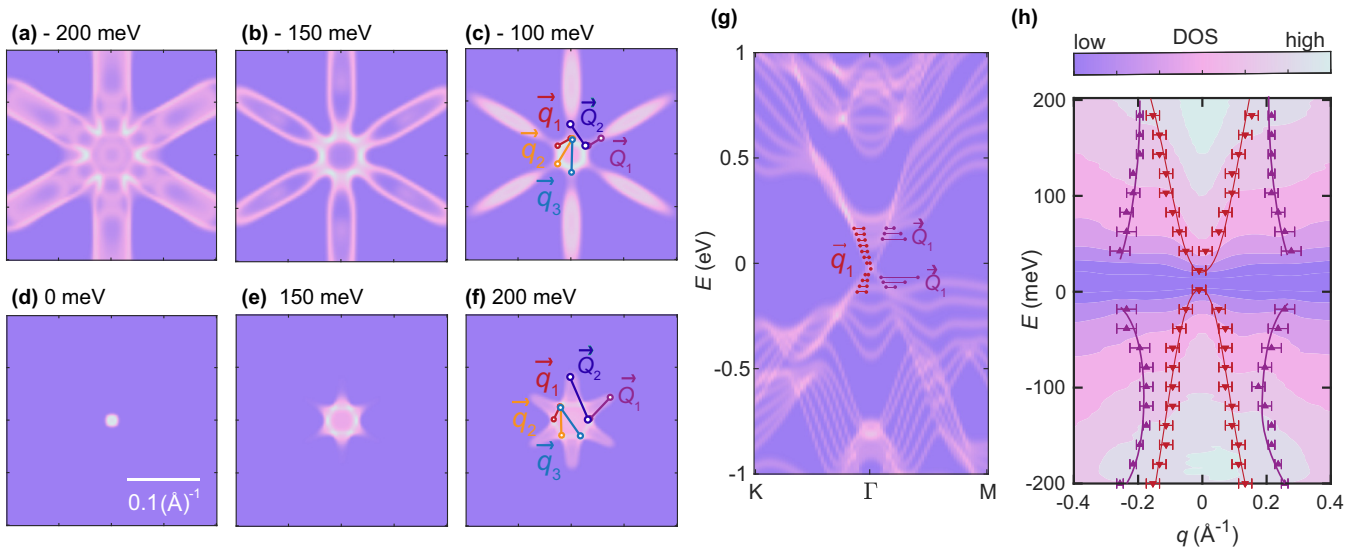


FIG. 8. Comparison of the calculated and measured energy dependence of LDOS in momentum space. Calculated momentum-resolved LDOS at (a) $E = -200$ meV, (b) $E = -150$ meV, (c) $E = -100$ meV, (d) $E = 0$ meV, (e) $E = 150$ meV and (f) $E = 200$ meV. The horizontal axis in the maps is directed towards the K point and the vertical axis is directed toward the M point. Furthermore, the solid lines indicate the scattering vectors between pairs of high DOS regions on the map. (g) Calculated energy dependence of momentum resolved LDOS. The red solid lines indicate the energy evolution of \vec{q}_1 and the purple solid lines indicate the evolution of \vec{Q}_1 . (h) A contour plot of the energy dependence of the measured QPI images taken along the M- Γ -M plane. The (red) ∇ symbols indicate the locations of the \vec{q}_1 scattering wave vectors, and the (purple) Δ symbols indicate the location of the \vec{Q}_1 scattering wave vectors.

By stacking up dI/dV maps of each bias voltages and taking a slice across the E - q plane, an energy-dependent contour map is obtained [Fig. 8(h)]. The energy dependence of $|\vec{q}_1|$ can be derived from this E - q contour plot across the M- Γ -M direction. Evidently, $|\vec{q}_1|$ in the M direction contracts as the energy evolves from below E_F and then expands as the energy increases above E_F , which is in accordance with the energy dependence of the radius of the surface-state Dirac cone [Fig. 8(g)], thus, further verifying the identification of the \vec{q}_1 scattering wave vector of the QPI maps.

Although the QPI maps also show clear defect-mediated surface-to-bulk scattering at energies of 100 meV above and below E_F , the absence of \vec{Q}_1 close to E_F asserts that quasiparticles are largely confined to within the surface near E_F , and bulk states are well separated from the Fermi level. We can consequently rule out the possibility of significant bulk states contributing to the impairment of quantized transport.

IV. DISCUSSIONS

A. Role of defects in spatial modulations of Δ_s

Both point spectroscopy and QPI analyses suggest that the bulk bands are well separated from the surface bands, granting direct thermal excitation of electrons either from bulk to bulk or from bulk to surface states on a local scale energetically unfavorable at least at 4.2 K. Rather than being inherent in the magnitude of Δ_s , spatial map of Δ_s indicates that the problem of vanishing QAHE at slightly elevated temperature lies in its spatial alignment of energy bands. Given that the average surface gap of the sample is approximately 13.5 meV, local modulations in the sample due to inhomogeneous doping, defects, or impurities of a few meVs lead to misalignment of the surface energy bands, allowing for tunneling of electrons from the surface valence band of a particular point to the surface conduction band of another separate point. Indeed, it is found that the energy of the surface conduction band in one region can be lower than the surface valence band in another region as shown in Fig. 9(c).

To discern the origin of the observed energy modulation, the spatial distribution of $E_{s,v}$ was compared with the positions of defects, revealed from the constant bias conductance map presented in Fig. 7(a). Given that quasiparticles experience scattering off defects, these defects induce modulations in the conductance map, facilitating their detection, as depicted in Fig. 9(a). By cross referencing the locations of defects with the distribution of $E_{s,v}$ measured from the same area [Fig. 9(b)], a clear correlation emerges: the positions of defects align with distinct energy levels of $E_{s,v}$. Notably, the regions populated with defects coincide with lower-energy levels, as indicated by the green patches in Fig. 9(b).

This correlation strongly suggests that the observed modulations in local chemical potentials are a direct consequence of the inherent defects within the system, yielding a spatially modulated gap, as outlined in the schematic diagram of Figs. 9(d) and 9(e).

As means of verifying the presence of a leaky current running along the surface state due to the energy modulation of bands, the tunneling probability of electrons across the topological surface as a function of disorder is numerically investigated in a finite superlattice Hamiltonian of pristine

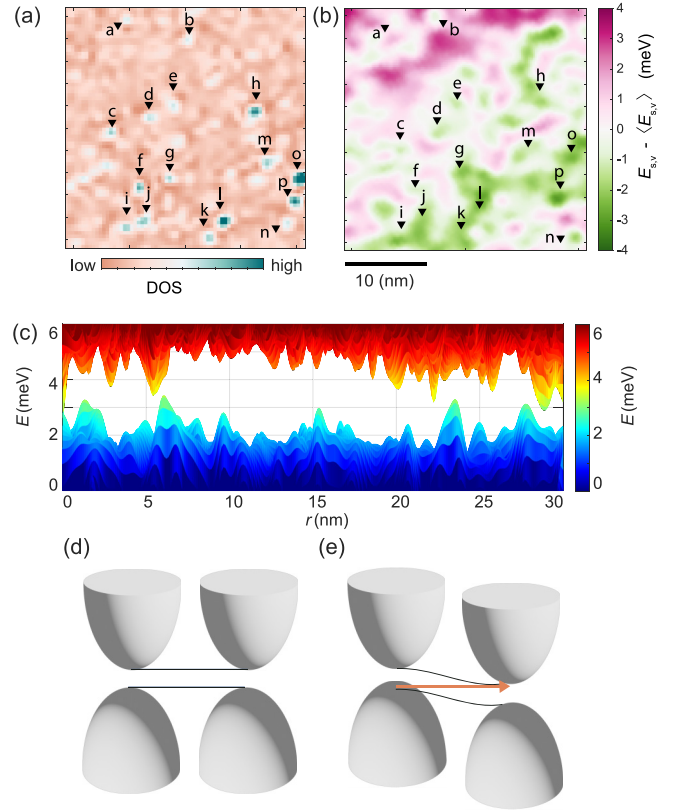


FIG. 9. Spatial profile of the topological surface gap. (a) A constant bias conductance map corresponding to an energy of $E = -150$ meV. The arrows point to representative defect locations found in this area. (b) A spatial distribution map of $E_{s,v}$ with respect to its average, $\langle E_{s,v} \rangle$ in the same area of (a). The arrows indicate local minima in the $\langle E_{s,v} \rangle$ and the approximate defect location of the defects labeled in (a). (c) Projection of a surface plot depicting the spatial profile of the topography and (b) its corresponding spatial profile of $E_{s,v}$ and $E_{s,c}$ obtained from STS scans over a 30 nm region at $T = 4.2$ K. Although the average surface gap at each point in the area is 13.5 meV, the spatial profile exhibits an effectively smaller gap owing to the energy modulations. Schematic diagram illustrating (d) an ideal case in which the surface gap through space are all aligned, and for (e) the case in which spatial modulations in $E_{s,v}$ and $E_{s,c}$ can allow indirect gap hopping, yielding an effectively gapless metallic phase on a nanoscale range at $T = 4.2$ K.

Sb_2Te_3 . Although there are various forms of defects in the sample including Sb/Te vacancies, antisites, typically in MBE grown samples, the concentration of such is 10^{-4} nm^{-2} [36], which is significantly dilute than the concentration of dopant atoms. For this reason, the main source of disorder within a nanometer scale region comes from Cr and Bi dopants, which have vastly different atomic mass and orbital characters from atoms in Sb_2Te_3 compound [45]. The effect of disorder generated by the dopant atoms are incorporated by emulating the shift in the local chemical potential $[\delta\mu^\alpha, (\alpha = \text{Cr}, \text{Bi})]$ introduced through Sb-site substitution. Since each Sb-site orbital has six orbitals (three p orbitals for each spin configuration), each dopant shifts the chemical potential for all six orbitals at each Sb site.

Assuming an RKKY interaction, in this model each orbital of the Cr dopant contributes to a z component in flux

density with a $B_z \propto r^{-3}$ dependence from its Wannier center in the radial direction [46]. Given that the Wannier orbitals of Cr dopants substitute a total of N_{Cr} number of Sb-site orbitals located at \vec{R}_i , each Cr-dopant orbital can be approximated to collectively contribute to a superposition of flux density,

$$B_z(\vec{r}) = B_{z0} \sum_i^{N_{\text{Cr}}} \left(\frac{1 - e^{-|\vec{r}-\vec{R}_i|/r_0}}{|\vec{r}-\vec{R}_i|/r_0} \right) \hat{r}, \quad (1)$$

where B_{z0} is the maximum flux density induced by a single local spin polarization and r_0 is the range of the magnetic exchange interaction, which is set to be $r_0 = 15$ nm [46]. A single dopant therefore creates a nearly uniform field, given that r_0 is substantially longer than the lattice parameter, spanning over 30 times the width of a unit cell. The magnetic field coming from Cr dopants has two effects: (i) induces spin-energy splitting through Zeeman interaction, as well as (ii) altering the electron motion through a Peierl's substitution. Not only contributing to magnetization, Cr dopants also have an effect of altering the Fermi level with respect to the Dirac point, which is reflected in the theoretical model as a shift in the on-site energy (ε_{ii}). For Cr dopants, this shift is approximately $\delta\mu^{\text{Cr}}(\vec{r}) = +150$ meV, as revealed through ARPES and STS studies [45,47]. Furthermore, to enforce a ferromagnetic insulating state [48], hopping to Cr dopants are prohibited in the model. All in all, the change in Hamiltonian owing to magnetic dopants is

$$\begin{aligned} \hat{H}^{\text{Cr}}(\vec{B}) = & \sum_i^N g_{\parallel} \mu_B B_z(\vec{r}) \psi_i^{\dagger} \sigma_z \psi_i + \sum_{i'}^{N_{\text{Cr}}} \delta\mu^{\text{Cr}}(\vec{r}) \psi_i^{\dagger} \psi_{i'} \\ & + \sum_{i'}^{N_{\text{Cr}}} \sum_{i \neq j}^N t_{ij} \cdot e^{i\Theta_{ij}} (\psi_i^{\dagger} \psi_j + \psi_j^{\dagger} \psi_i) (1 - \delta_{ii'}), \quad (2) \end{aligned}$$

where g_{\parallel} is the Landè g factor parallel to the crystal c axis, which is approximately 25 generally for 3D topological insulators [49,50], t_{ij} is the hopping energy, and Θ_{ij} is the Peierl's phase, given by

$$\Theta_{ij} = \frac{h}{e} \int_{\vec{R}_i}^{\vec{R}_j} \vec{r} \times \vec{B} \cdot d\vec{r}. \quad (3)$$

For the case of Bi dopants, which do not contribute to magnetization, only the on-site energies are altered and the hopping terms are left untouched

$$\hat{H}^{\text{Bi}}(\vec{r}) = \sum_{i'}^{N_{\text{Bi}}} \delta\mu^{\text{Bi}}(\vec{r}) \psi_i^{\dagger} \psi_{i'}. \quad (4)$$

Here N_{Bi} represents the number of Wannier orbitals of the Sb site substituted with the Wannier orbitals of the Bi dopants, and the shift in the on-site energy is $\delta\mu^{\text{Bi}} = -100$ meV, determined through ARPES measurements [33].

Figure 10 exhibits the band structures of Sb_2Te_3 in the limit where there is uniform magnetic field threaded through the lattice and in the case in which there are no disorder. As the magnetic field increases, degeneracy of the bands are lifted and a band inversion occurs at around a flux density of $B = 6$ T [Figs. 10(a) and 10(c)], thus giving rise to a magnetic gap at higher fields. This critical field at which a

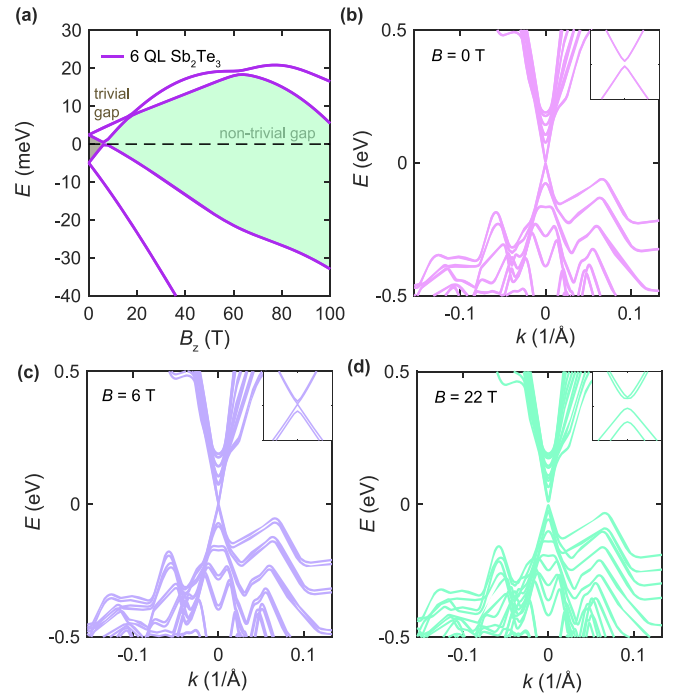


FIG. 10. Surface gap dependence of magnetic field in six QL Sb_2Te_3 . (a) The evolution of the lowest two conduction bands and the highest two valence bands as a function of magnetic field. The corresponding band structure of six QL Sb_2Te_3 along the K- Γ -M path at (b) $B = 0$ T, (c) $B = 6$ T, where the gap closes, and (d) $B = 22$ T where a topologically nontrivial magnetic gap is observed. The inset exhibits a blowup of the low-energy region, in which the vertical axis scales from -50 to 50 meV and the horizontal axis scales from -0.01 \AA^{-1} to 0.01 \AA^{-1} .

band inversion occurs is consistent to the order of magnitude of the critical field $B_C \approx 20 \text{ meV}/(25 \mu_B) \approx 10$ T computed by a four-band model of 5QL Bi_2Se_3 topological insulator thin film [48]. With a field reaching $B \approx 22$ T, the magnetic gap is ≈ 15 meV, which is approximately about the magnitude of Δ_s experimentally seen at 4.2 K. Notably, even with extreme magnetic fields of 100 T, the magnetic gap only reaches as high as ≈ 40 meV.

Likewise, three-QL Sb_2Te_3 also shows a band inversion but at a higher field of $B = 40$ T owing to larger hybridization gap that necessitates a larger Zeeman splitting (Fig. 11). The size of the surface gap is smaller in general compared to the six-QL case. At a higher field of 50 T, the gap reaches a magnitude ≈ 10 meV, however, the surface bands are less separated from the bulk bands [Fig. 11(d)]. Thus, incorporating a field within a window larger than $B = 40$ T, but less than $B = 50$ T ensures a QAH-phase in the three-QL system in which the surface is well separated from the bulk states. Given the correspondence between the three-QL and the six-QL systems, the effects of disorder and phonon coupling can therefore be estimated in the QAHE-phase of a three-QL system and then compared to experimental results of six-QL samples to maintain reasonable computational costs.

Effects of disorder were implemented to a finite ($10 \times 10 \times 1$) superlattice three-QL system consisting of 1500 atoms ($N = 9000$ total orbitals) and randomly replacing the

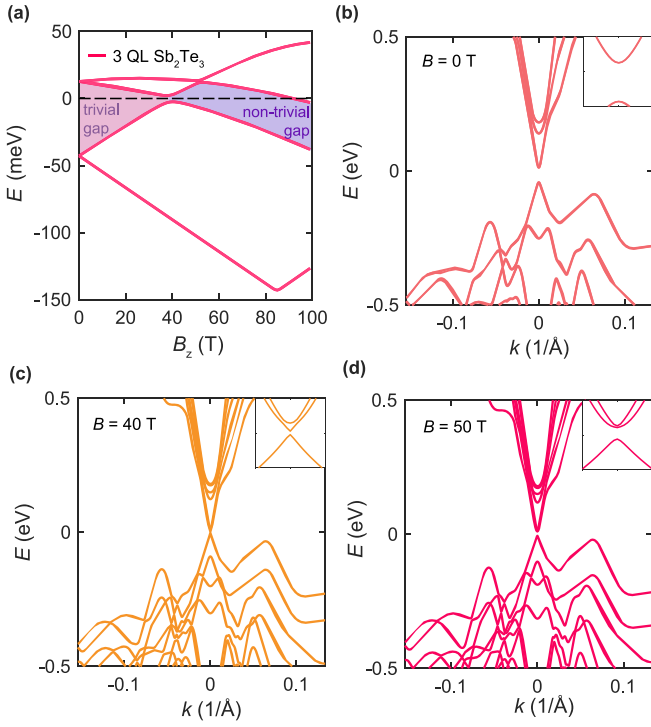


FIG. 11. Surface gap dependence of magnetic field in 3 QL Sb_2Te_3 . (a) The evolution of the lowest two conduction bands and the highest two valence bands as a function of magnetic field. The corresponding band structure of 3 QL Sb_2Te_3 along the K- Γ -M path at (b) $B = 0$ T, (c) $B = 40$ T, where the gap closes, and (d) $B = 50$ T where a topologically nontrivial magnetic gap is observed. The inset exhibits a blowup of the low-energy region, in which the vertical axis scales from -50 to 50 meV and the horizontal axis scales from -0.01 \AA^{-1} to 0.01 \AA^{-1} .

orbitals of Sb sites with 108 Bi dopants ($x = 0.8$, $N_{\text{Bi}} = 648$) and 60 Cr dopants ($y = 0.1$, $N_{\text{Cr}} = 360$), where each Cr orbital contributes to a flux density of $B_0 = 0.125$ T (such that the average total flux density $\langle B_z \rangle \approx 45$ T). To assess the effects of modulations in local chemical potential owing to the dopants to the chiral edge states, we compare the spatial distribution of the surface state probability density in the finite lattice of two cases, (i) nondoped QAH-phase: no dopants ($N_{\text{Bi}} = N_{\text{Cr}} = 0$, yet in the QAH state by turning on magnetization with $B_z = 45$ T), and (ii) doped QAH phase the case with both Bi and Cr dopants matching the stoichiometry of $\text{Cr}_{0.1}(\text{Bi}_{0.2}\text{Sb}_{0.8})_{1.9}\text{Te}_3$.

Specifically, this is visualized by plotting the probability density of all the edge eigenstates ($|\psi_e|^2$) within an energy window of ± 5 meV from E_F ,

$$|\psi_e(\vec{r}_i)\rangle = \sum_{\substack{|E_n - E_F| \\ < 5\text{meV}}} |\psi_n(\vec{r}_i)\rangle. \quad (5)$$

In the lattice without any dopants, states within this 10 meV energy frame where the topological gap is located is predominantly clustered near the edge and virtually no states towards the center of the crystal (Fig. 12). As defects are incorporated [Fig. 12(b)], patches of substantial $|\psi_e|^2$ are observed in the

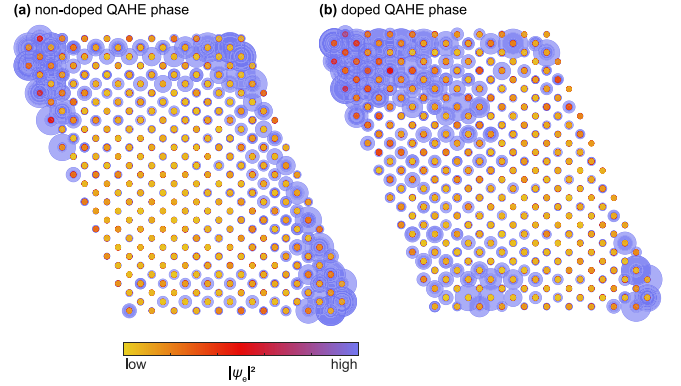


FIG. 12. A bubble chart depicting the edge state probability density $|\psi_e|^2$ in a $(10 \times 10 \times 1)$ 3 QL finite lattice at their corresponding Wannier centers projected along the crystal ab plane (a) without any defects (i.e., $N_{\text{Bi}} = N_{\text{Cr}} = 0$ but in the QAH state by turning on magnetization with $B_z = 45$ T), and (b) 108 Bi dopants and 60 Cr dopants (i.e., $N_{\text{Bi}} = 648$ and $N_{\text{Cr}} = 360$ with $\langle B_z \rangle \approx 45$ T).

interior of the crystal. Therefore, dopants play a role in modulating energies of eigenstates close to E_F .

B. Role of phonon mediated band renormalization

The theory of topological insulators has been built upon a noninteracting quasiparticle framework. However, when putting into consideration effects of finite temperature, which cannot be neglected in experiments, there is no escape from recognizing many-body interactions [51]. In particular, at finite temperatures, electron-phonon (e - p) interactions are dominant scattering mechanism of the surface state Dirac electrons [52]. Inclusion of an e - p term in the Hamiltonian of the system can consequently renormalize the electronic band structure in topological insulators [53]. Although there is no consensus on the e - p coupling strength between phonons and the topological surface states due to its experimental difficulties [51–60], experimental methods including ARPES have directly observed phonon scattering in the surface states [51,52,59,60].

Figure 13 exhibits the phonon spectrum of the bulk and slab geometry of Sb_2Te_3 . Since there are five atoms in a primitive unit cell, there are 15 phonon modes, in which three

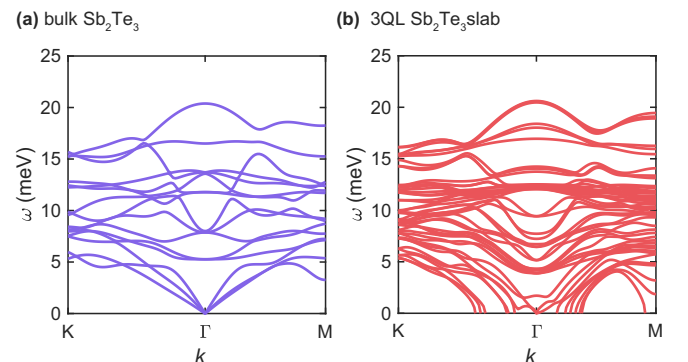


FIG. 13. Phonon spectrum along the K- Γ -M path of Sb_2Te_3 for (a) a primitive cell and (b) a 3 QL slab geometry.

are low-energy acoustic modes, and 12 are higher-energy optical modes. To study the e - p interactions among the surface states, phonons were calculated for a three-QL slab geometry [Fig. 13(b)]. In a three-QL slab, there are a total of 15 atoms, resulting in a sum of 45 phonon modes. There are numerous acoustic modes that extend below zero frequency, which reflect imaginary phonon modes emerging from anharmonicity. Usually, the existence of imaginary modes is associated with dynamical instabilities such as the Jahn-Teller instability. However, the rise of imaginary phonon modes in this specific case can be considered a result of phonon anharmonicity with the presence of a vacuum above and below the slab geometry in which the phonon modes were calculated.

The electron-phonon interaction to the first order is expressed as

$$\hat{H}^{ep}(\vec{r}) = \frac{1}{M\sqrt{N}} \sum_{\vec{k}\vec{q}} \sum_{mnv} g_{mnv}(\vec{k}, \vec{q}) c_{m, \vec{k}+\vec{q}}^\dagger c_{n, \vec{k}} x_{qv}, \quad (6)$$

where $x_{q,v} = a_{v, -\vec{q}} + a_{v, -\vec{q}}^\dagger$ is the bosonic displacement operator [61]. Moreover, M is the total number of bands, N is the number of unit cells, c^\dagger and c (a^\dagger and a) are the associated fermionic (bosonic) creation and annihilation operators for electrons (phonons), respectively. Notably, this is a single-phonon absorption/emission process in which momentum is conserved and the amount of energy transfer between the electron and phonon is denoted by the coupling matrix g_{mnv} .

Through a change of basis by Fourier transforming creation/annihilation operators into field operators,

$$c_{m, \vec{k}}^\dagger = \frac{1}{\sqrt{N}} \sum_i \psi_m^\dagger(\vec{r}_i) e^{+i(\vec{k}+\vec{q})\cdot\vec{r}_i} \quad (7)$$

$$c_{n, \vec{k}} = \frac{1}{\sqrt{N}} \sum_j \psi_n(\vec{r}_j) e^{-i\vec{k}\cdot\vec{r}_j}, \quad (8)$$

the real-space Hamiltonian is represented as

$$\hat{H}^{ep}(\vec{r}) = \frac{1}{MN\sqrt{N}} \sum_{i,j} \sum_{mnv} g_{mnv}(\vec{r}_i, \vec{r}_j) \psi_m^\dagger(\vec{r}_i) \psi_n(\vec{r}_j), \quad (9)$$

where the electron-phonon coupling matrix element in the lattice representation is

$$g_{mnv}(\vec{r}_i, \vec{r}_j) = \sum_{\vec{k}\vec{q}} g_{mnv} e^{i\vec{k}\cdot(\vec{r}_i-\vec{r}_j)+i\vec{q}\cdot\vec{r}_i} \Delta x_{qv}. \quad (10)$$

Given that the linear component of electron-phonon interactions is irrelevant to band renormalization [62], we consider that in thermal equilibrium the phonon interaction rather coming from phonon displacement x_{qv} , emanates from the variance $\Delta x_{qv} = \sqrt{\langle x^2 \rangle - \langle x \rangle^2} = \sqrt{\hbar\omega_{\text{ph}} n_{\text{BE}}}$, thereby accounting for fluctuations in atomic displacement. Here, $n_{\text{BE}} = 1/(e^{\hbar\omega_{\text{ph}}/k_{\text{B}}T} + 1)$ is the Bose-Einstein distribution function, expressing the phonon population. Using the e - p coupling constant g_{mnv} obtained through DPFT calculations, temperature-dependent effects on the surface states were computed.

As the temperature of the system increases from 0 to 10 K, a recognizable reduction of meV order in Δ_s is observed (Fig. 14). Within this temperature range, Δ_s remains gapped,

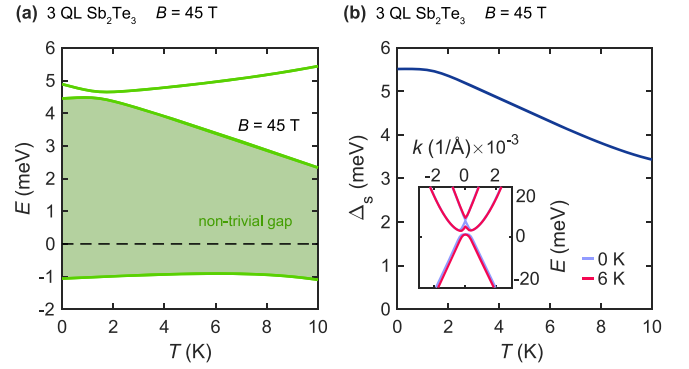


FIG. 14. Effects of e - p renormalization on the surface state band structure. (a) The temperature dependence of surface valence and conduction bands of 3 QL Sb_2Te_3 with a magnetic field of 45 T to create a QAH phase. (b) The temperature dependence of Δ_s . The inset shows the surface state band structure around the Γ point for $T = 0$ K and $T = 6$ K.

implying that at liquid- ^4He temperature of 4.2 K, QAH phase is present (Fig. 14). Nonetheless, such renormalization effect, which induces a gap reduction, augments vulnerability of the system to rise of leaky currents due to disorder-induced spatial energy modulations of the eigenstates.

C. Combined effects of electron-phonon interaction and disorder on surface band renormalization

In experimental reality, finite-temperature effects and disorder are simultaneously present. To take both into account, Eq. (6) and Eq. (2) are introduced as perturbations, such that the fully integrated Hamiltonian is

$$\hat{H}(\vec{B}, T) = \sum_{i,j}^N \varepsilon_{ij} \psi_i^\dagger \psi_j + \hat{H}^{\text{Cr}}(\vec{B}) + \hat{H}^{\text{Bi}}(\vec{r}) + \hat{H}^{ep}(T), \quad (11)$$

which is implemented to study the collective effects of disorder and e - p interactions on a $(5 \times 5 \times 1)$ finite superlattice of three-QL Sb_2Te_3 .

Whether electrons can tunnel through inhomogeneous puddles of states that form inside the topological surface gap owing to such many-body interaction is assessed through calculating the transfer matrix $T_{\text{I,II}}$ for electrons from one edge (I) reaching to the opposite edge (II), as illustrated in Fig. 15(a). For both the nondoped QAH phase and doped QAH phase, the transfer matrix $T_{\text{I,II}}$ is given by

$$T_{\text{I,II}} = \text{Tr}[\hat{\rho}(t)\rho_{\text{II}}] = \text{Tr}[\hat{U}\hat{\rho}_\text{I}\hat{U}^\dagger\hat{\rho}_\text{II}]. \quad (12)$$

Here the density operators, $\hat{\rho}_\text{I}$ and ρ_II , express the edge state of surface-state orbitals on edge I and edge II,

$$\hat{\rho}_\text{I} = \frac{1}{N_\text{I}} \sum_{\substack{|E_n - E_\text{F}| \\ < 5\text{meV}}} \sum_{\text{I}} |\psi_n(\vec{r}_\text{I})\rangle \langle \psi_n(\vec{r}_\text{I})| \quad (13)$$

$$\hat{\rho}_\text{II} = \frac{1}{N_\text{II}} \sum_{\substack{|E_n - E_\text{F}| \\ < 5\text{meV}}} \sum_{\text{II}} |\psi_n(\vec{r}_\text{II})\rangle \langle \psi_n(\vec{r}_\text{II})|, \quad (14)$$

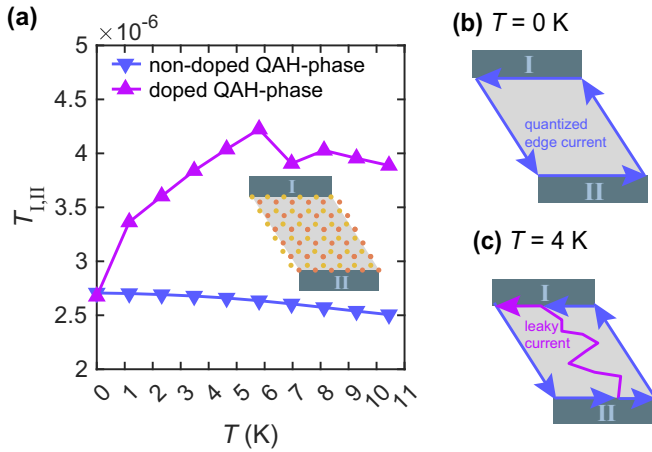


FIG. 15. Effects of e - p renormalization on the surface state band structure. (a) $T_{I,II}$ as a function of temperature with no dopants yet in the QAHE state owing to application of magnetization of $B_z = 45$ T and incorporation of 15 Bi dopants and 27 Cr dopants with $\langle B_z \rangle = 45$ T to emulate the stoichiometry of $\text{Cr}_{0.1}(\text{Bi}_{0.2}\text{Sb}_{0.8})_{1.9}\text{Te}_3$. The inset illustrates a schematic diagram of the $(5 \times 5 \times 1)$ superlattice for calculating probability that an electron can be transmitted across the crystal from edge I to II. (b) A schematic diagram illustrating quantized transport at $T = 0$ K, and (c) compromised quantized transport at finite temperatures as a consequence of both defect and phonon mediated metal transition.

where $\hat{U}_n = e^{-iE_n t/\hbar} |\psi_n\rangle \langle \psi_n|$ is the unitary time-evolution operator of the n th eigenstate. The time scale t is set to a value large enough to allow for $T_{I,II}$ to saturate to its maximum for all temperature ranges. Figure 15(a) exhibits that by excluding dopants, the transmission probability across the device is virtually unchanged with increasing temperatures. In other words, the role of e - p interactions by itself is not sufficient for granting surface state mediate leakage of electron from edge I to edge II. Intriguingly, upon incorporating defects into the system, a considerable gain in transmission from edge I to edge II is attained at finite temperatures, implying that both defects and e - p interactions are necessary ingredients for the deterioration of quantized transport in $\text{Cr}_y(\text{Bi}_{1-x}\text{Sb}_x)_{2-y}\text{Te}_3$ [Figs. 15(b) and 15(c)].

V. CONCLUSION

There are three echelons of dimensionality in transport in MTIs: bulk (3D), surface (2D), and edge (1D) modes, in which the 1D edge states are responsible for the QAHE. Lack of quantized transport either proceeds from destruction of the edge modes, and/or leakage of current from the bulk and/or surface. Observation of a topological nontrivial gap above sub-Kelvin temperature rules out the possibility of annihilation of chiral edge states being the culprit, which also has been demonstrated by prior transport studies [19,63,64]. Moreover, since STS measurements indicate that the bulk states are energetically well separated from the edge states, such circumstance is unlikely as well. Thus, our detailed STS studies narrow down the perpetrator to be the leakage within the surface states.

We have revealed in this work that there are spatial modulations in surface conduction and valence bands on the meV scale. Given that the two bands are only separated by ≈ 13.5 meV (at 4.2 K), slight spatial modulations in bands can give rise to regions in which the valence band maximum is higher than the conduction band minimum at a different point separated by < 3 nm distance within the sample. The presence of energy misalignment in Δ_s is a facet of both (i) disorder particularly owing to Bi and Cr dopants in the Sb_2Te_3 system and (ii) electron-phonon interaction of the surface states. Numerical calculations presented here indicate that although increasing the number of Bi and Cr dopants alone result in an increase in transmission of electrons across the spatially modulated surface bands, there is a further surge when incorporating the effects electron-phonon interactions. Such detrimental effect of e - p interactions emanates from its renormalization effect to the surface band such that the magnitude of Δ_s is reduced at finite temperatures. Consequently, the effects of disorder-induced spatial band modulations intensify, yielding a higher degree of leaky current to tunnel across the gap. Notably, the effects of phonons alone are not strong enough to generate an effective gapless state without the role of disorder. Only when combining both effects together, an effectively gapless phase is created, which results in leakage currents throughout the surface state along with the existing edge states, thus shrouding the QAHE. Although we have numerically simulated the effects of Bi and Cr dopants, we can expect the same for V dopants, as they also induce a shift in the local chemical potential.

In other words, suppressing either one of disorder or e - p interactions would allow for QAHE at elevated temperatures. Unfortunately, owing to the futility of attempting to engineer e - p interactions for a known crystalline structure, a method of growing samples with a spatially highly uniform Dirac point and a perfect alignment of the Fermi energy with the Dirac point will be necessary to align the topological surface gap spatially so as to improve the quantum transport properties of MTIs, at least for the $\text{Cr}_y(\text{Bi}_{1-x}\text{Sb}_x)_{2-y}\text{Te}_3$ system. With the recent development of the capability of an intrinsic antiferromagnetic topological insulator, MnBi_2Te_4 , to exhibit quantized transport at a temperature of 1.4 K at zero field in a five septuple layer sample without the need of any doping [65], moreover with a larger surface gap of 60–85 meV [66,67], MnBi_2Te_4 can be considered as a compelling platform. Yet, up to date, QAHE in these materials have been limited to exfoliated nanoflakes due to the lack of capability in growing well-engineered MBE thin films. Efforts towards synthesizing thin films of MnBi_2Te_4 that exhibit quantized transport at elevated temperatures are still needed towards realistic technological applications based on the QAHE [68–70].

ACKNOWLEDGMENTS

The authors gratefully acknowledge joint support for this work by the Army Research Office (US) under the MURI program (Award No. W911NF-16-1-0472), National Science Foundation (US) (Award No. 1733907) under the Physics Frontier Centers program for the Institute for Quantum Information and Matter (IQIM) at the California Institute of

Technology, and the Kavli Foundation. N.-C.Y. acknowledges partial support from the Thomas W. Hogan Professorship at Caltech, the Yushan Fellowship awarded by the Ministry of

Education in Taiwan, and the Yushan Fellow Distinguished Professorship at the National Taiwan Normal University (TW) in Taiwan.

- [1] C.-Z. Chang, J. Zhang, X. Feng, J. Shen, Z. Zhang, M. Guo, K. Li, Y. Ou, P. Wei, L.-L. Wang, Z.-Q. Ji, Y. Feng, S. Ji, X. Chen, J. Jia, X. Dai, Z. Fang, S.-C. Zhang, K. He, Y. Wang *et al.*, Experimental observation of the quantum anomalous Hall effect in a magnetic topological insulator, *Science* **340**, 167 (2013).
- [2] X. Kou, S.-T. Guo, Y. Fan, L. Pan, M. Lang, Y. Jiang, Q. Shao, T. Nie, K. Murata, J. Tang, Y. Wang, L. He, T.-K. Lee, W.-L. Lee, and K. L. Wang, Scale-invariant quantum anomalous Hall effect in magnetic topological insulators beyond the two-dimensional limit, *Phys. Rev. Lett.* **113**, 137201 (2014).
- [3] J. G. Checkelsky, R. Yoshimi, A. Tsukazaki, K. S. Takahashi, Y. Kozuka, J. Falson, M. Kawasaki, and Y. Tokura, Trajectory of the anomalous Hall effect towards the quantized state in a ferromagnetic topological insulator, *Nat. Phys.* **10**, 731 (2014).
- [4] P. P. J. Haazen, J.-B. Laloë, T. J. Nummy, H. J. M. Swagten, P. Jarillo-Herrero, D. Heiman, and J. S. Moodera, Ferromagnetism in thin-film Cr-doped topological insulator Bi_2Se_3 , *Appl. Phys. Lett.* **100**, 082404 (2012).
- [5] S. Grauer, S. Schreyeck, M. Winnerlein, K. Brunner, C. Gould, and L. W. Molenkamp, Coincidence of superparamagnetism and perfect quantization in the quantum anomalous Hall state, *Phys. Rev. B* **92**, 201304(R) (2015).
- [6] X. Feng, Y. Feng, J. Wang, Y. Ou, Z. Hao, C. Liu, Z. Zhang, L. Zhang, C. Lin, J. Liao, Y. Li, L.-L. Wang, S.-H. Ji, X. Chen, X. Ma, S.-C. Zhang, Y. Wang, K. He, and Q.-K. Xue, Thickness dependence of the quantum anomalous Hall effect in magnetic topological insulator films, *Adv. Mater.* **28**, 6386 (2016).
- [7] I. Lee, C. K. Kim, J. Lee, S. J. L. Billinge, R. Zhong, J. A. Schneeloch, T. Liu, T. Valla, J. M. Tranquada, G. Gu, and J. C. S. Davis, Imaging Dirac-mass disorder from magnetic dopant atoms in the ferromagnetic topological insulator $\text{Cr}_x(\text{Bi}_{0.1}\text{Sb}_{0.9})_{2-x}\text{Te}_3$, *Proc. Natl. Acad. Sci.* **112**, 1316 (2015).
- [8] E. O. Lachman, A. F. Young, A. Richardella, J. Cuppens, H. R. Naren, Y. Anahory, A. Y. Meltzer, A. Kandala, S. Kempinger, Y. Myasoedov, M. E. Huber, N. Samarth, and E. Zeldov, Visualization of superparamagnetic dynamics in magnetic topological insulators, *Sci. Adv.* **1**, e1500740 (2015).
- [9] M. Mogi, R. Yoshimi, A. Tsukazaki, K. Yasuda, Y. Kozuka, K. S. Takahashi, M. Kawasaki, and Y. Tokura, Magnetic modulation doping in topological insulators toward higher-temperature quantum anomalous Hall effect, *Appl. Phys. Lett.* **107**, 182401 (2015).
- [10] Y. Ou, C. Liu, G. Jiang, Y. Feng, D. Zhao, W. Wu, X.-X. Wang, W. Li, C. Song, L.-L. Wang, W. Wang, W. Wu, Y. Wang, K. He, X.-C. Ma, and Q.-K. Xue, Enhancing the quantum anomalous Hall effect by magnetic codoping in a topological insulator, *Adv. Mater.* **30**, 1703062 (2018).
- [11] C.-Z. Chang, P. Tang, Y.-L. Wang, X. Feng, K. Li, Z. Zhang, Y. Wang, L.-L. Wang, X. Chen, C. Liu, W. Duan, K. He, X.-C. Ma, and Q.-K. Xue, Chemical-potential-dependent gap opening at the Dirac surface states of Bi_2Se_3 induced by aggregated substitutional Cr atoms, *Phys. Rev. Lett.* **112**, 056801 (2014).
- [12] C.-C. Chen, M. L. Teague, L. He, X. Kou, M. Lang, W. Fan, N. Woodward, K.-L. Wang, and N.-C. Yeh, Magnetism-induced massive Dirac spectra and topological defects in the surface state of Cr-doped Bi_2Se_3 -bilayer topological insulators, *New J. Phys.* **17**, 113042 (2015).
- [13] L. Zhang, D. Zhao, Y. Zang, Y. Yuan, G. Jiang, M. Liao, D. Zhang, K. He, X. Ma, and Q. Xue, Ferromagnetism in vanadium-doped Bi_2Se_3 topological insulator films, *APL Mater.* **5**, 076106 (2017).
- [14] Y. L. Chen, J.-H. Chu, J. G. Analytis, Z. K. Liu, K. Igarashi, H.-H. Kuo, X. L. Qi, S. K. Mo, R. G. Moore, D. H. Lu, M. Hashimoto, T. Sasagawa, S. C. Zhang, I. R. Fisher, Z. Hussain, and Z. X. Shen, Massive Dirac fermion on the surface of a magnetically doped topological insulator, *Science* **329**, 659 (2010).
- [15] C. K. Kim, J. D. Denlinger, A. K. Kundu, G. Gu, and T. Valla, Absence of a Dirac gap in ferromagnetic $\text{Cr}_x(\text{Bi}_{0.1}\text{Sb}_{0.9})_{2-x}\text{Te}_3$, *J. Appl. Phys.* **129**, 083902 (2021).
- [16] E. Golias, E. Weschke, T. Flanagan, E. Schierle, A. Richardella, E. D. L. Rienks, P. S. Mandal, A. Varykhalov, J. Sánchez-Barriga, F. Radu, N. Samarth, and O. Rader, Magnetization relaxation and search for the magnetic gap in bulk-insulating V-doped $(\text{Bi}, \text{Sb})_2\text{Te}_3$, *Appl. Phys. Lett.* **119**, 132404 (2021).
- [17] P. Sessi, R. R. Biswas, T. Bathon, O. Storz, S. Wilfert, A. Barla, K. A. Kokh, O. E. Tereshchenko, K. Fauth, M. Bode, and A. V. Balatsky, Dual nature of magnetic dopants and competing trends in topological insulators, *Nat. Commun.* **7**, 12027 (2016).
- [18] A. M. Black-Schaffer, A. V. Balatsky, and J. Fransson, Filling of magnetic-impurity-induced gap in topological insulators by potential scattering, *Phys. Rev. B* **91**, 201411(R) (2015).
- [19] C.-Z. Chang, W. Zhao, D. Y. Kim, P. Wei, J. K. Jain, C. Liu, M. H. W. Chan, and J. S. Moodera, Zero-field dissipationless chiral edge transport and the nature of dissipation in the quantum anomalous Hall state, *Phys. Rev. Lett.* **115**, 057206 (2015).
- [20] W. Li, M. Claassen, C.-Z. Chang, B. Moritz, T. Jia, C. Zhang, S. Rebec, J. J. Lee, M. Hashimoto, D.-H. Lu, R. G. Moore, J. S. Moodera, T. P. Devereaux, and Z.-X. Shen, Origin of the low critical observing temperature of the quantum anomalous Hall effect in V-doped $(\text{Bi}, \text{Sb})_2\text{Te}_3$ film, *Sci. Rep.* **6**, 32732 (2016).
- [21] L. Pan, X. Liu, Q. L. He, A. Stern, G. Yin, X. Che, Q. Shao, P. Zhang, P. Deng, C.-Y. Yang, B. Casas, E. S. Choi, J. Xia, X. Kou, and K. L. Wang, Probing the low-temperature limit of the quantum anomalous Hall effect, *Sci. Adv.* **6**, eaaz3595 (2020).
- [22] X. Kou, L. Pan, J. Wang, Y. Fan, E. S. Choi, W.-L. Lee, T. Nie, K. Murata, Q. Shao, S.-C. Zhang, and K. L. Wang, Metal-to-insulator switching in quantum anomalous Hall states, *Nat. Commun.* **6**, 8474 (2015).
- [23] Y. X. Chong, X. Liu, R. Sharma, A. Kostin, G. Gu, K. Fujita, J. C. S. Davis, and P. O. Sprau, Severe Dirac mass gap suppression in Sb_2Te_3 -based quantum anomalous Hall materials, *Nano Lett.* **20**, 8001 (2020).
- [24] H.-Z. Lu, A. Zhao, and S.-Q. Shen, Quantum transport in magnetic topological insulator thin films, *Phys. Rev. Lett.* **111**, 146802 (2013).
- [25] Yeh, N.-C., Teague, M. L., Wu, R. T.-P., Chu, H., Boyd, D. A., Bockrath, M. W., He, L., Xiu, F.-X., and wang, K.-L.,

- Scanning tunnelling spectroscopic studies of Dirac fermions in graphene and topological insulators, *EPJ Web Conf.* **23**, 00021 (2012).
- [26] Y. Zhang, K. He, C.-Z. Chang, C.-L. Song, L.-L. Wang, X. Chen, J.-F. Jia, Z. Fang, X. Dai, W.-Y. Shan, S.-Q. Shen, Q. Niu, X.-L. Qi, S.-C. Zhang, X.-C. Ma, and Q.-K. Xue, Crossover of the three-dimensional topological insulator Bi_2Se_3 to the two-dimensional limit, *Nat. Phys.* **6**, 584 (2010).
- [27] P. Giannozzi, S. Baroni, N. Bonini, M. Calandra, R. Car, C. Cavazzoni, D. Ceresoli, G. L. Chiarotti, M. Cococcioni, I. Dabo, A. D. Corso, S. de Gironcoli, S. Fabris, G. Fratesi, R. Gebauer, U. Gerstmann, C. Gougoussis, A. Kokalj, M. Lazzeri, L. Martin-Samos *et al.*, Quantum espresso: A modular and open-source software project for quantum simulations of materials, *J. Phys.: Condens. Matter* **21**, 395502 (2009).
- [28] P. Giannozzi, O. Andreussi, T. Brumme, O. Bunau, M. B. Nardelli, M. Calandra, R. Car, C. Cavazzoni, D. Ceresoli, M. Cococcioni, N. Colonna, I. Carnimeo, A. D. Corso, S. de Gironcoli, P. Delugas, R. A. DiStasio Jr, A. Ferretti, A. Floris, G. Fratesi, G. Fugallo *et al.*, Advanced capabilities for materials modelling with quantum espresso, *J. Phys.: Condens. Matter* **29**, 465901 (2017).
- [29] A. A. Mostofi, J. R. Yates, G. Pizzi, Y.-S. Lee, I. Souza, D. Vanderbilt, and N. Marzari, An updated version of wannier90: A tool for obtaining maximally-localised Wannier functions, *Comput. Phys. Commun.* **185**, 2309 (2014).
- [30] H. Zhang, C.-X. Liu, X.-L. Qi, X. Dai, Z. Fang, and S.-C. Zhang, Topological insulators in Bi_2Se_3 , Bi_2Te_3 and Sb_2Te_3 with a single Dirac cone on the surface, *Nat. Phys.* **5**, 438 (2009).
- [31] Q. Wu, S. Zhang, H.-F. Song, M. Troyer, and A. A. Soluyanov, Wanniertools: An open-source software package for novel topological materials, *Comput. Phys. Commun.* **224**, 405 (2018).
- [32] S. Ponc e, E. Margine, C. Verdi, and F. Giustino, EPW: Electron-phonon coupling, transport and superconducting properties using maximally localized wannier functions, *Comput. Phys. Commun.* **209**, 116 (2016).
- [33] J. Zhang, C.-Z. Chang, Z. Zhang, J. Wen, X. Feng, K. Li, M. Liu, K. He, L. Wang, X. Chen, Q.-K. Xue, X. Ma, and Y. Wang, Band structure engineering in $(\text{Bi}_{1-x}\text{Sb}_x)_2\text{Te}_3$ ternary topological insulators, *Nat. Commun.* **2**, 574 (2011).
- [34] K. L. Scipioni, Z. Wang, Y. Maximenko, F. Katmis, C. Steiner, and V. Madhavan, Role of defects in the carrier-tunable topological-insulator $(\text{Bi}_{1-x}\text{Sb}_x)_2\text{Te}_3$ thin films, *Phys. Rev. B* **97**, 125150 (2018).
- [35] F. Yang, Y. R. Song, H. Li, K. F. Zhang, X. Yao, C. Liu, D. Qian, C. L. Gao, and J.-F. Jia, Identifying magnetic anisotropy of the topological surface state of $\text{Cr}_{0.05}\text{Sb}_{1.95}\text{Te}_3$ with spin-polarized stm, *Phys. Rev. Lett.* **111**, 176802 (2013).
- [36] Y. Jiang, Y. Y. Sun, M. Chen, Y. Wang, Z. Li, C. Song, K. He, L. Wang, X. Chen, Q.-K. Xue, X. Ma, and S. B. Zhang, Fermi-level tuning of epitaxial Sb_2Te_3 thin films on graphene by regulating intrinsic defects and substrate transfer doping, *Phys. Rev. Lett.* **108**, 066809 (2012).
- [37] J. Gooth, R. Zierold, P. Sergelius, B. Hamdou, J. Garcia, C. Damm, B. Rellinghaus, H. J. Pettersson, A. Pertsova, C. Canali, M. Borg, and K. Nielsch, Local magnetic suppression of topological surface states in Bi_2Te_3 nanowires, *ACS Nano* **10**, 7180 (2016).
- [38] S. Buchenau, S. Scheitz, A. Sethi, J. E. Slimak, T. E. Glier, P. K. Das, T. Dankwort, L. Akinsinde, L. Kienle, A. Rusydi, C. Ulrich, S. L. Cooper, and M. R ubhausen, Temperature and magnetic field dependent raman study of electron-phonon interactions in thin films of Bi_2Se_3 and Bi_2Te_3 nanoflakes, *Phys. Rev. B* **101**, 245431 (2020).
- [39] H. Beidenkopf, P. Roushan, J. Seo, L. Gorman, I. Drozdov, Y. S. Hor, R. J. Cava, and A. Yazdani, Spatial fluctuations of helical Dirac fermions on the surface of topological insulators, *Nat. Phys.* **7**, 939 (2011).
- [40] W.-C. Lee, C. Wu, D. P. Arovas, and S.-C. Zhang, Quasiparticle interference on the surface of the topological insulator Bi_2Te_3 , *Phys. Rev. B* **80**, 245439 (2009).
- [41] Y. Okada, C. Dhital, W. Zhou, E. D. Huemiller, H. Lin, S. Basak, A. Bansil, Y.-B. Huang, H. Ding, Z. Wang, S. D. Wilson, and V. Madhavan, Direct observation of broken time-reversal symmetry on the surface of a magnetically doped topological insulator, *Phys. Rev. Lett.* **106**, 206805 (2011).
- [42] T. Zhang, P. Cheng, X. Chen, J.-F. Jia, X. Ma, K. He, L. Wang, H. Zhang, X. Dai, Z. Fang, X. Xie, and Q.-K. Xue, Experimental demonstration of topological surface states protected by time-reversal symmetry, *Phys. Rev. Lett.* **103**, 266803 (2009).
- [43] S. Zhu, Y. Ishida, K. Kuroda, K. Sumida, M. Ye, J. Wang, H. Pan, M. Taniguchi, S. Qiao, S. Shin, and A. Kimura, Ultrafast electron dynamics at the Dirac node of the topological insulator Sb_2Te_3 , *Sci. Rep.* **5**, 13213 (2015).
- [44] J. Reimann, J. G udde, K. Kuroda, E. V. Chulkov, and U. H ofer, Spectroscopy and dynamics of unoccupied electronic states of the topological insulators Sb_2Te_3 and $\text{Sb}_2\text{Te}_2\text{S}$, *Phys. Rev. B* **90**, 081106(R) (2014).
- [45] Y. Jiang, C. Song, Z. Li, M. Chen, R. L. Greene, K. He, L. Wang, X. Chen, X. Ma, and Q.-K. Xue, Mass acquisition of Dirac fermions in magnetically doped topological insulator Sb_2Te_3 films, *Phys. Rev. B* **92**, 195418 (2015).
- [46] Q. Liu, C.-X. Liu, C. Xu, X.-L. Qi, and S.-C. Zhang, Magnetic impurities on the surface of a topological insulator, *Phys. Rev. Lett.* **102**, 156603 (2009).
- [47] W. Zhang, D. West, S. H. Lee, Y. Qiu, C.-Z. Chang, J. S. Moodera, Y. S. Hor, S. Zhang, and W. Wu, Electronic fingerprints of Cr and V dopants in the topological insulator Sb_2Te_3 , *Phys. Rev. B* **98**, 115165 (2018).
- [48] R. Yu, W. Zhang, H.-J. Zhang, S.-C. Zhang, X. Dai, and Z. Fang, Quantized anomalous Hall effect in magnetic topological insulators, *Science* **329**, 61 (2010).
- [49] A. Wolos, S. Szyszko, A. Drabinska, M. Kaminska, S. G. Strzelecka, A. Hruban, A. Materna, M. Piersa, J. Borysiuk, K. Sobczak, and M. Konczykowski, g -factors of conduction electrons and holes in Bi_2Se_3 three-dimensional topological insulator, *Phys. Rev. B* **93**, 155114 (2016).
- [50] V. Sakhin, E. Kukovitsky, Y. Talanov, and G. Teitelbaum, To the inhomogeneous bulk state of the $\text{Bi}_{1.08}\text{Sn}_{0.02}\text{Sb}_{0.9}\text{Te}_2\text{S}$ topological insulator as revealed by ESR of charge carriers, *JETP Lett.* **113**, 273 (2021).
- [51] R. Heid, I. Y. Sklyadneva, and E. V. Chulkov, Electron-phonon coupling in topological surface states: The role of polar optical modes, *Sci. Rep.* **7**, 1095 (2017).
- [52] X. Zhu, L. Santos, C. Howard, R. Sankar, F. C. Chou, C. Chamon, and M. El-Batanouny, Electron-phonon coupling on the surface of the topological insulator Bi_2Se_3 determined from

- surface-phonon dispersion measurements, *Phys. Rev. Lett.* **108**, 185501 (2012).
- [53] I. Garate, Phonon-induced topological transitions and crossovers in Dirac materials, *Phys. Rev. Lett.* **110**, 046402 (2013).
- [54] R. C. Hatch, M. Bianchi, D. Guan, S. Bao, J. Mi, B. B. Iversen, L. Nilsson, L. Hornekær, and P. Hofmann, Stability of the $\text{Bi}_2\text{Se}_3(111)$ topological state: Electron-phonon and electron-defect scattering, *Phys. Rev. B* **83**, 241303(R) (2011).
- [55] Z.-H. Pan, A. V. Fedorov, D. Gardner, Y. S. Lee, S. Chu, and T. Valla, Measurement of an exceptionally weak electron-phonon coupling on the surface of the topological insulator Bi_2Se_3 using angle-resolved photoemission spectroscopy, *Phys. Rev. Lett.* **108**, 187001 (2012).
- [56] T. Kondo, Y. Nakashima, Y. Ota, Y. Ishida, W. Malaeb, K. Okazaki, S. Shin, M. Kriener, S. Sasaki, K. Segawa, and Y. Ando, Anomalous dressing of Dirac fermions in the topological surface state of Bi_2Se_3 , Bi_2Te_3 , and Cu-doped Bi_2Se_3 , *Phys. Rev. Lett.* **110**, 217601 (2013).
- [57] S. Giraud, A. Kundu, and R. Egger, Electron-phonon scattering in topological insulator thin films, *Phys. Rev. B* **85**, 035441 (2012).
- [58] G. Benedek, S. Miret-Artés, J. R. Manson, A. Ruckhofer, W. E. Ernst, and A. Tamtögl, Origin of the electron-phonon interaction of topological semimetal surfaces measured with helium atom scattering, *J. Phys. Chem. Lett.* **11**, 1927 (2020).
- [59] W. Richter and C. R. Becker, A Raman and far-infrared investigation of phonons in the rhombohedral $\text{V}_2\text{-VI}_3$ compounds Bi_2Te_3 , Bi_2Se_3 , Sb_2Te_3 and $\text{Bi}_2(\text{Te}_{1-x}\text{Se}_x)_3(0 < x < 1)$, $(\text{Bi}_{1-y}\text{Sb}_y)_2\text{Te}_3(0 < y < 1)$, *Physica Status Solidi B* **84**, 619 (1977).
- [60] J. A. Sobota, S.-L. Yang, D. Leuenberger, A. F. Kemper, J. G. Analytis, I. R. Fisher, P. S. Kirchmann, T. P. Devereaux, and Z.-X. Shen, Distinguishing bulk and surface electron-phonon coupling in the topological insulator Bi_2Se_3 using time-resolved photoemission spectroscopy, *Phys. Rev. Lett.* **113**, 157401 (2014).
- [61] F. Giustino, Electron-phonon interactions from first principles, *Rev. Mod. Phys.* **89**, 015003 (2017).
- [62] P. B. Allen and V. Heine, Theory of the temperature dependence of electronic band structures, *J. Phys. C* **9**, 2305 (1976).
- [63] K. Yasuda, T. Morimoto, R. Yoshimi, M. Mogi, A. Tsukazaki, M. Kawamura, K. S. Takahashi, M. Kawasaki, N. Nagaosa, and Y. Tokura, Large non-reciprocal charge transport mediated by quantum anomalous Hall edge states, *Nat. Nanotechnol.* **15**, 831 (2020).
- [64] K. M. Fijalkowski, N. Liu, P. Mandal, S. Schreyeck, K. Brunner, C. Gould, and L. W. Molenkamp, Quantum anomalous Hall edge channels survive up to the Curie temperature, *Nat. Commun.* **12**, 5599 (2021).
- [65] Y. Deng, Y. Yu, M. Z. Shi, Z. Guo, Z. Xu, J. Wang, X. H. Chen, and Y. Zhang, Quantum anomalous Hall effect in intrinsic magnetic topological insulator MnBi_2Te_4 , *Science* **367**, 895 (2020).
- [66] M. M. Otrokov, I. I. Klimovskikh, H. Bentmann, D. Estyunin, A. Zeugner, Z. S. Aliev, S. Gaß, A. U. B. Wolter, A. V. Koroleva, A. M. Shikin, M. Blanco-Rey, M. Hoffmann, I. P. Rusinov, A. Y. Vyazovskaya, S. V. Ereemeev, Y. M. Koroteev, V. M. Kuznetsov, F. Freyse, J. Sánchez-Barriga, I. R. Amiraslanov *et al.*, Prediction and observation of an antiferromagnetic topological insulator, *Nature (London)* **576**, 416 (2019).
- [67] S. H. Lee, Y. Zhu, Y. Wang, L. Miao, T. Pillsbury, H. Yi, S. Kempinger, J. Hu, C. A. Heikes, P. Quarterman, W. Ratcliff, J. A. Borchers, H. Zhang, X. Ke, D. Graf, N. Alem, C.-Z. Chang, N. Samarth, and Z. Mao, Spin scattering and non-collinear spin structure-induced intrinsic anomalous Hall effect in antiferromagnetic topological insulator MnBi_2Te_4 , *Phys. Rev. Res.* **1**, 012011(R) (2019).
- [68] N. Liu, S. Schreyeck, K. Fijalkowski, M. Kamp, K. Brunner, C. Gould, and L. Molenkamp, Antiferromagnetic order in MnBi_2Te_4 films grown on $\text{Si}(111)$ by molecular beam epitaxy, *J. Cryst. Growth* **591**, 126677 (2022).
- [69] S.-H. Su, J.-T. Chang, P.-Y. Chuang, M.-C. Tsai, Y.-W. Peng, M. K. Lee, C.-M. Cheng, and J.-C. A. Huang, Epitaxial growth and structural characterizations of MnBi_2Te_4 thin films in nanoscale, *Nanomaterials* **11**, 3322 (2021).
- [70] Y.-F. Zhao, L.-J. Zhou, F. Wang, G. Wang, T. Song, D. Ovchinnikov, H. Yi, R. Mei, K. Wang, M. H. W. Chan, C.-X. Liu, X. Xu, and C.-Z. Chang, Even-odd layer-dependent anomalous Hall effect in topological magnet MnBi_2Te_4 thin films, *Nano Lett.* **21**, 7691 (2021).